Electronic Supplementary Material (ESI) for Energy & Environmental Science.
This journal is © The Royal Society of Chemistry 2024

Supporting Information

Electronic Structure Optimization of Metal-Phthalocyanine via Confining Atomic Ru for All-pH Hydrogen Evolution

Zhenhui Kou,[a,c] Yingnan Liu,[a] Wenjun Cui,[g] Bin Yang,[a] Zhongjian Li,[a] Raul D. Rodriguez,[e] Qinghua Zhang,[a] Chung-Li Dong,[f] Xiahan Sang,[g] Lecheng Lei,[a] Tao Zhang,[c*] and Yang Hou[a,b,d*]

[a]College of Chemical and Biological Engineering, Zhejiang University, Hangzhou, Zhejiang 310027, China

[b]Institute of Zhejiang University - Quzhou, Quzhou, 324000, China

[c]Key Laboratory of Marine Materials and Related Technologies, Ningbo Institute of Materials Technology and Engineering, Chinese Academy of Sciences, Ningbo 315201, China

[d]Donghai Laboratory, Zhoushan, 316021, China

[e]Tomsk Polytechnic University, 30 Lenin Ave, Tomsk 634050, Russia

[f]Research Center for X-ray Science & Department of Physics, Tamkang University, New Taipei City, 25 137 Taiwan

[g]Research and Testing Centre of Material School of Materials Science and Engineering, Wuhan University of Technology, 430070, Wuhan, China

Experimental section

Synthesis of bulk-phase NiFe PPc

2.0 g of pyromellitic dianhydride, 4.4 g of urea, 1.0 g of NH_4Cl, 30 mg of $(NH_4)_6Mo_7O_{24}\cdot 4H_2O$ and a certain amount of $NiCl_2\cdot 6H_2O$ and $FeCl_3$ was grinded evenly in mortar. Then, the ground product was transferred to magnetic boat and further heated and calcinated at 210 °C at a ramp rate of 3 °C min^{-1} and maintained for 3 h in a muffle furnace. After cooling down to room temperature, the product was washed several times through water, acetone, and ethanol. The obtained sediment was dried at 60 °C more than 12 h under vacuum condition.

Synthesis of 2D NiFe PPc

The electrochemical exfoliation was performed by a two-electrode system, in which bulk-phase NiFe PPc was used as cathode and Pt foil was used as anode. 250 mg of tetrabutylammonium bromide and 50 mL of acetonitrile were put into a 150 mL beaker and stirred evenly to serve as electrolyte. The electrochemical exfoliation process was performed at a voltage of -5.0 V within 60 min. After complete exfoliation, the delaminated NiFe PPc was washed six times using centrifuge treatment at 8000 rpm for washing products. Afterwards, final product of 2D NiFe PPc can be dispersed through a mild sonication method in ice bath.

Synthesis of Ru_{SA}@NiFe PPc

The Ru_{SA}@NiFe PPc was synthesized by an electrochemical deposition strategy, during which the 2D NiFe PPc fixed on the carbon paper as working electrode, and the electrolyte contained the 0.5 M H_2SO_4 with a certain amount of $(NH_4)RuCl_6$. And then, the electrodeposition process procced through changing the polarization cycles in electrochemical system at a scan rate of 20 mV s^{-1} between 0 and -0.6 V vs. RHE.

Characterizations

The morphologies of as-prepared catalysts were examined by a field-emission scanning electron microscope (FESEM, Hitachi SU-8010), transmission electron microscope (TEM, HT7700), and high-resolution transmission electron microscopy (HRTEM, JEOL JEM-2100F). The Ru single atom feature was measured by aberration-corrected scanning transmission electron microscopy (Titan Cubed Themis

G2 300) and XAS measurements were performed at the BL17C station in Taiwan Synchrotron Radiation Research Center. The crystal structures of as-prepared catalysts were measured by X-ray diffraction (XRD) (Empyrean 200895) using Cu Kα radiation. The chemical environments of as-prepared catalysts were measured by X-ray photoelectron spectroscopy (XPS) spectra (Escalab 250Xi) with an Al Kα radiation. The thickness of as-prepared catalysts was measured by AFM (MultiMode of VEECO). Raman spectra of as-prepared catalysts were performed by a Laser confocal Raman instrument (Horiba Jobin Yvon, LabRAM HR Evolution). Inductively coupled plasma tests were performed by SPECTRO ARCOS (ICP-OES).

Electrochemical measurements

All electrochemical measurements were carried out by an electrochemical analyzer (CHI 760E) in a typical three-electrode configuration at 298 K. A saturated Ag/AgCl electrode and a graphite rod were used as reference electrode and counter electrode, respectively. To prepare catalyst ink, 10 mg of electrocatalyst was evenly dispersed into 900 μL of ethanol and 100 μL of 0.5 wt.% Nafion solution, and then 50 μL of ink was dropped onto the 1 x 1 cm^2 carbon paper with a loading amount of 0.5 mg cm^{-2}, which was acted as working electrode. The potential was converted to reversible hydrogen electrode (RHE) *via* a Nernst equation ($E_{RHE} = E_{Ag/Ag/Cl} + 0.059 \times pH + 0.197$). To evaluate the HER activities of as-prepared catalysts, the scan rate of linear sweep voltammetry (LSV) was set to 5.0 mV s^{-1}. Electrochemical impedance spectroscopy (EIS) was measured at -1.035 V with a frequency range from 100 KHz to 0.01 Hz. For stability study, i-t measurement was tested at a current density of 100 mA cm^{-2} in 1 M KOH applying voltage of -1.43 V, 50 mA cm^{-2} and 200 mA cm^{-2} in 0.5 M H_2SO_4 applying voltage of -0.335 V and -0.572 V, respectively. Electrochemical measurements of commercial Pt/C catalyst were carried out by electrochemical analyzer CHI 760E in a typical three-electrode configuration. A saturated Ag/AgCl electrode and a graphite rod were used as reference electrode and counter electrode, respectively. To prepare Pt/C catalyst ink, 10 mg of Pt/C was evenly dispersed into 900 μL of ethanol and 100 μL of 0.5 wt.% Nafion solution, and then 50 μL of ink was dropped onto the 1 x 1 cm^2 carbon paper with a loading amount

of 0.5 mg cm^{-2}, acting as working electrode. The amount of Pt species was 20.0 wt.% in commercial Pt/C. To evaluate the HER activities of commercial Pt/C, linear sweep voltammetry (LSV) measurement proceeded from 0 V to -0.8 V vs. Ag/AgCl in 0.5 M H_2SO_4, and -0.8 V to -1.6 V vs. Ag/AgCl in 1.0 M KOH, with scan rate of 5.0 mV s^{-1}.

Electrochemical measurements for alkaline electrolyzer

Alkaline water electrolyzer consist cathode and anode plates, cathode and anode catalysts, diaphragm, and Teflon gasketing. Among them, Ru_{SA}@NiFe PPc, Pt/C, and Raney nickel was selected as cathode catalyst, respectively, as well as stainless steel mesh as anode cathode. A Zirfon Perl UTP 220 was utilized as diaphragm. The leakage of electrolyte was avoided by Teflon gaskets. The above cell components were compressed during installation to realize a zero-gap assembly reactor. The alkaline water electrolyzer were connected to electrochemical analyzer, while a peristaltic pump (LongerPump BT100-2J) continuously supplied the anodic and cathodic half-cells with a 30 wt.% KOH at a flow rate of 10 mL min^{-1}, at a temperature of 80 °C. The electrochemical results like that polarization curves were obtained through electrochemical analyzer. The assembly configuration of PEMWE was similar to alkaline electrolyzer, except that the diaphragm was replaced with proton exchange membrane (Nafion™ 117) and the electrolyte was replaced by 0.5 M H_2SO_4.

Computational details

The first-principle DFT calculations were performed by Vienna Ab initio Simulation Package[1] (VASP) with the projector augmented wave[2] (PAW) method. Perdew-Burke-Ernzerhof[3] (PBE) functional within the generalized gradient approximation[4] (GGA) was used to treat the exchange and correlation potential. The plane-wave cutoff energy level for all calculations was set to 500 eV and the force on each atom less than 0.03 eV $Å^{-1}$ was set for convergence criterion of geometry relaxation. The self-consistent field (SCF) tolerance level was 1.0×10^{-6} eV for the geometry optimization and electronic properties calculations. The k space was sampled with a Γ point centred at $2 \times 2 \times 1$ in geometry optimizations and at $4 \times 4 \times 1$ in electronic properties calculations for Ru@Ni PPc and Ru@Fe PPc. The Grimme method for

DFT-D3 was used to account for van der Waals (vdW) interactions.[5]

The periodic 2D models of geometrically optimized Ru@Ni PPc and Ru@Fe PPc were first built for energy and electronic properties calculations. A 15 Å vacuum was added along the z direction in order to avoid the interaction between periodic structures. The configuration of each adsorption intermediate was determined by comparing the energy of several different adsorption site structures after geometry optimizations. And the structure with the lowest energy was chosen in the calculation. The Gibbs free energy of the adsorbed state was calculated as follows formula:

$$G = E_0 + E_{ZPV} - TS$$

where E_0 is the absolute energy obtained by VASP, E_{ZPV} is the zero point vibration energy, T is the temperature (T = 298.15 K) and S is the entropy. The E_{ZPV} and the TS terms are obtained based on vibration analysis.

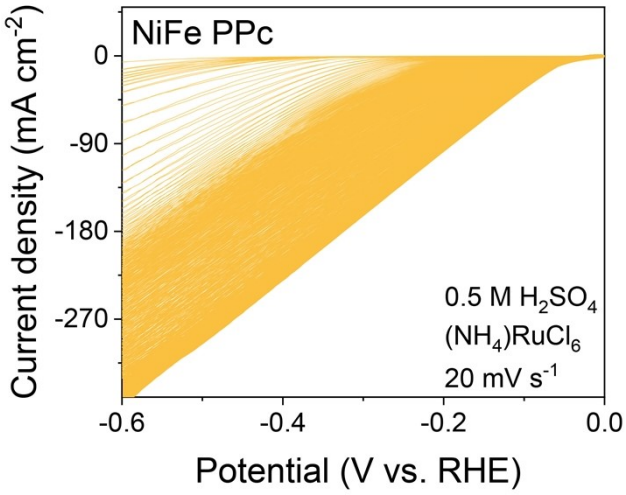

Figure S1. The CV curves of NiFe PPc.

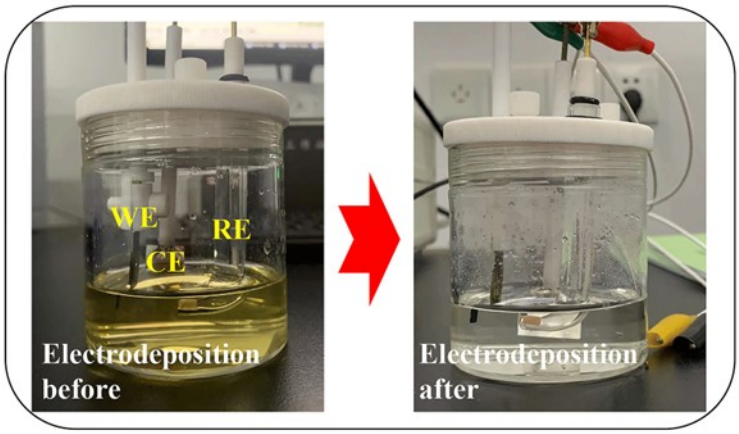

Figure S2. The optical photographs before and after electrochemical deposition process.

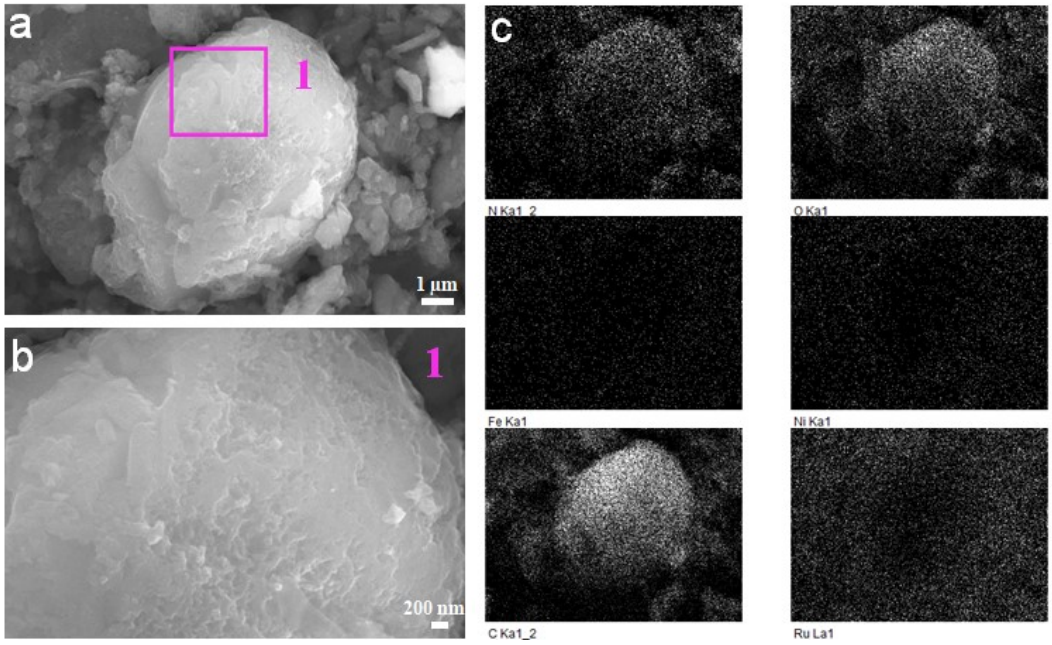

Figure S3. (a) FESEM and (b) enlarged FESEM image of Ru_{SA}@bulk-phase NiFe PPc. (c) EDX elemental mapping images of Ru_{SA}@bulk-phase NiFe PPc.

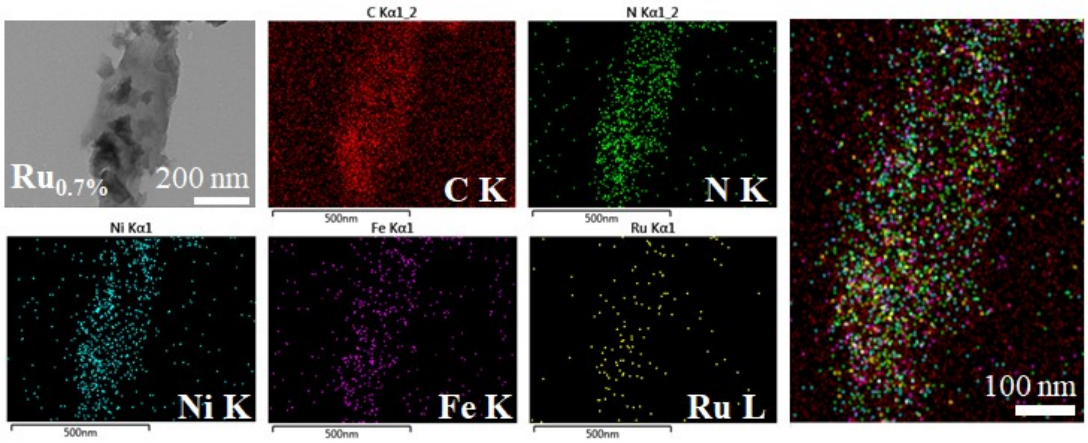

Figure S4. EDX elemental mapping images of Ru_{SA}@NiFe PPc.

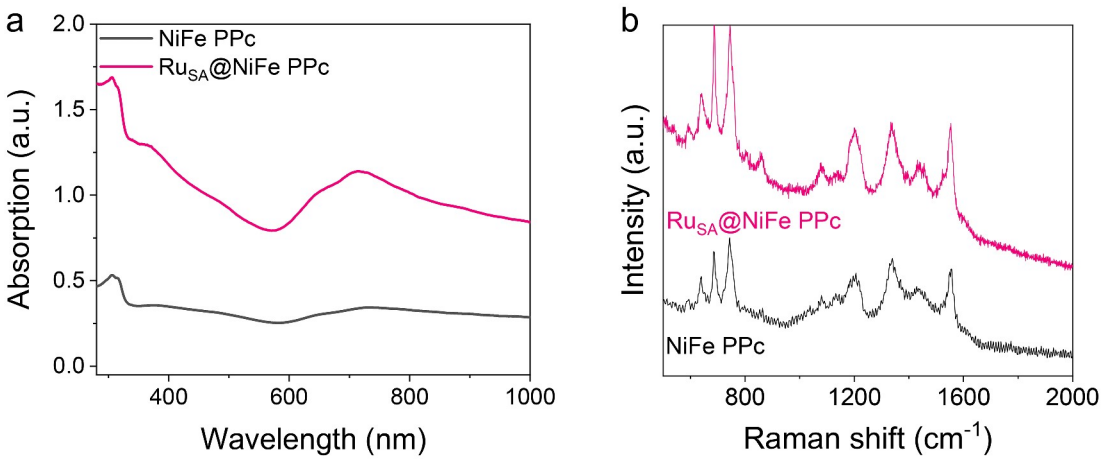

Figure S5. (a) UV-Vis absorption spectra of NiFe PPc and Ru_{SA}@NiFe PPc. (b) Raman spectra of NiFe PPc and Ru_{SA}@NiFe PPc.

The UV-Vis spectrum of Ru_{SA}@NiFe PPc showed two peaks ascribed to the characteristic peaks of Q-band (600 - 800 nm) and B-band (300 - 400 nm) of metal phthalocyanine structure, respectively, implying the NiFe PPc owned the pristine structure before and after incorporating Ru. Meanwhile, the comparison of vibration peaks of Ru_{SA}@NiFe PPc and NiFe PPc in the Raman spectra demonstrated that the Ru_{SA}@NiFe PPc still retained the original phthalocyanine-macrocycle structure, after the deposition in acid media.

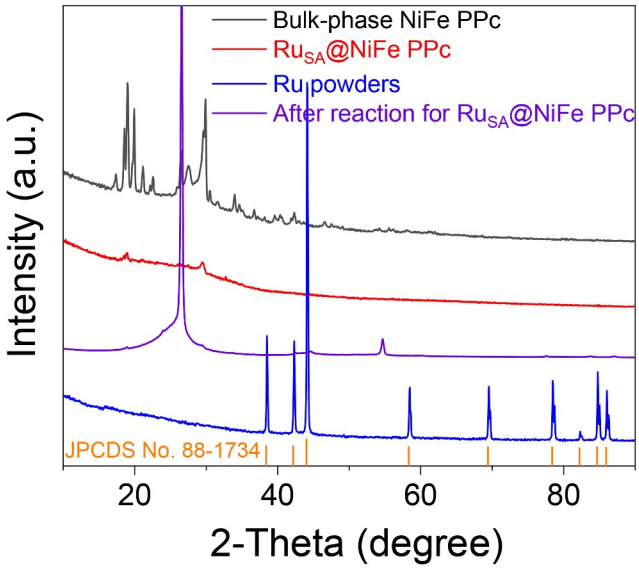

Figure S6. XRD patterns of bulk-phase NiFe PPc, Ru_{SA}@NiFe PPc, Ru powders, and Ru_{SA}@NiFe PPc after HER reaction.

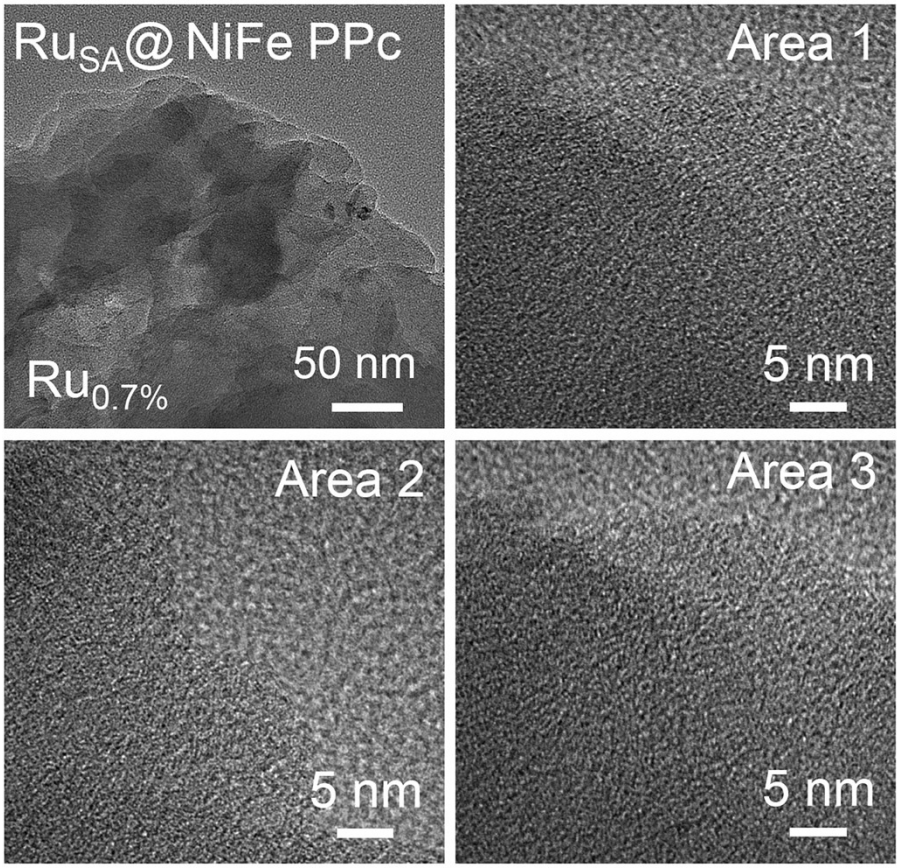

Figure S7. HRTEM images of Ru_{SA}@NiFe PPc.

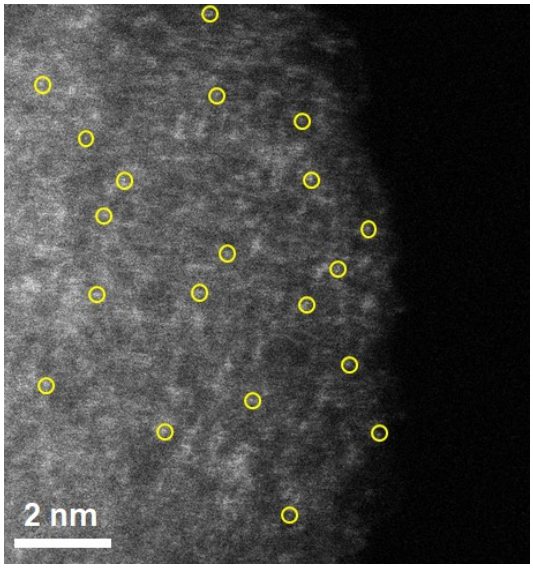

Figure S8. AC HAADF-STEM image of Ru_{SA}@NiFe PPc.

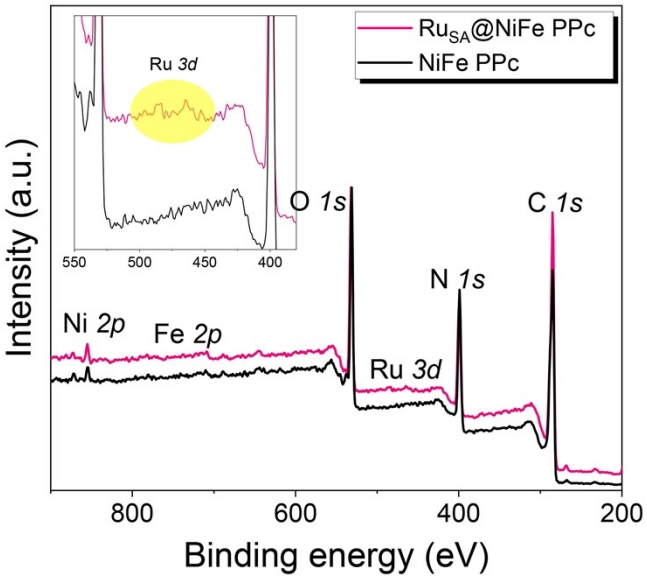

Figure S9. XPS survey spectra of Ru_{SA}@NiFe PPc and NiFe PPc.

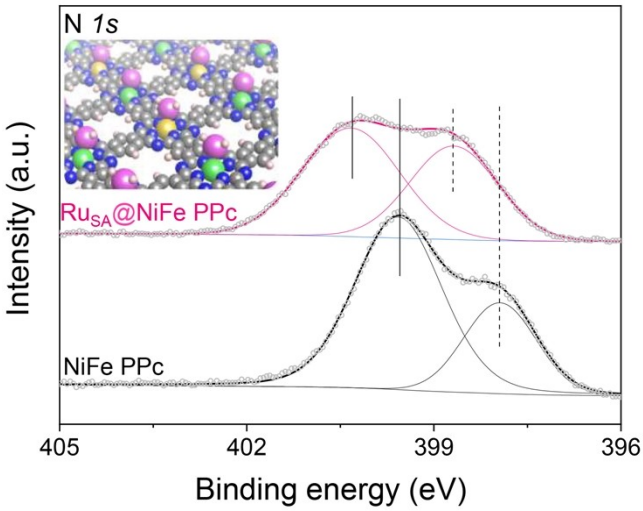

Figure S10. High-resolution N 1s XPS spectra of Ru_{SA}@NiFe PPc and NiFe PPc.

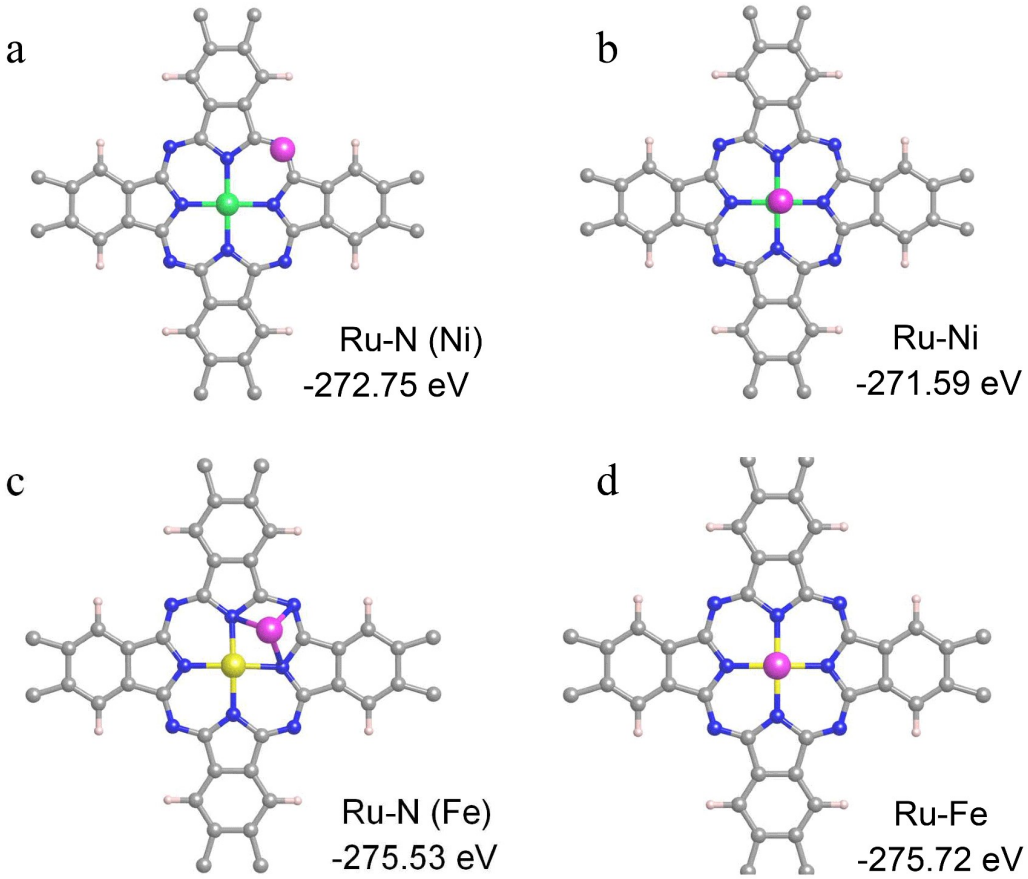

Figure S11. The diagrams for binding energy between Ru atoms and (a) N near Ni sites, (b) Ni sites, (c) N near Fe sites, and (d) Fe sites on NiFe PPc.

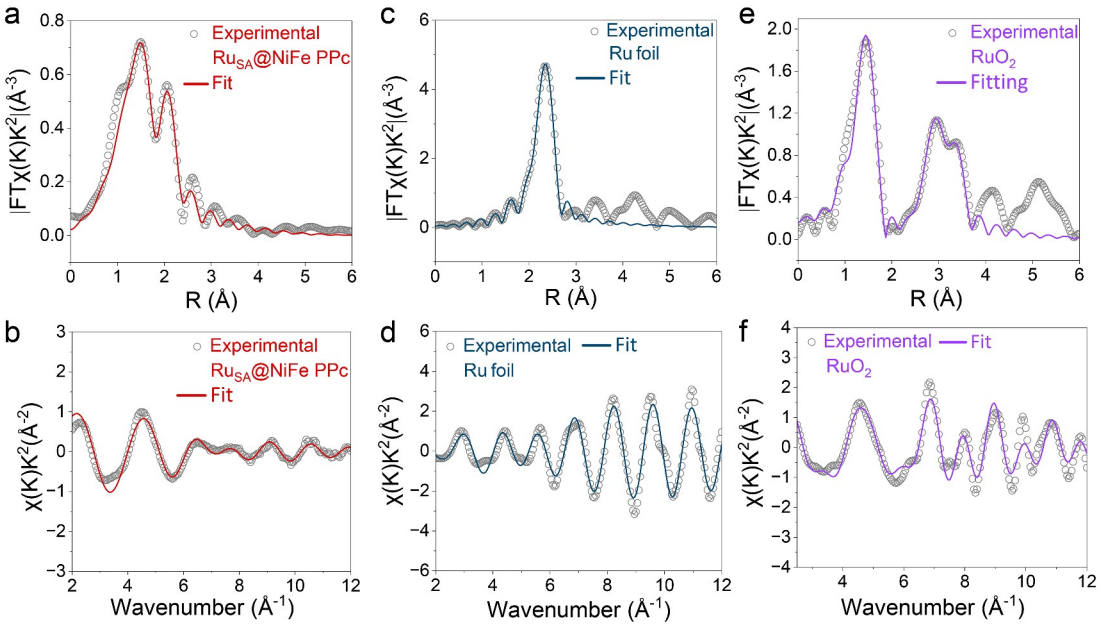

Figure S12. Fourier transform EXAFS fitting results of (a) Ru_{SA}@NiFe PPc, (c) Ru foil, and (e) RuO_2. Fourier transform of Ru K-edge EXAFS spectra in k space and corresponding fittings for (b) Ru_{SA}@NiFe PPc, (d) Ru foil, and (f) RuO_2.

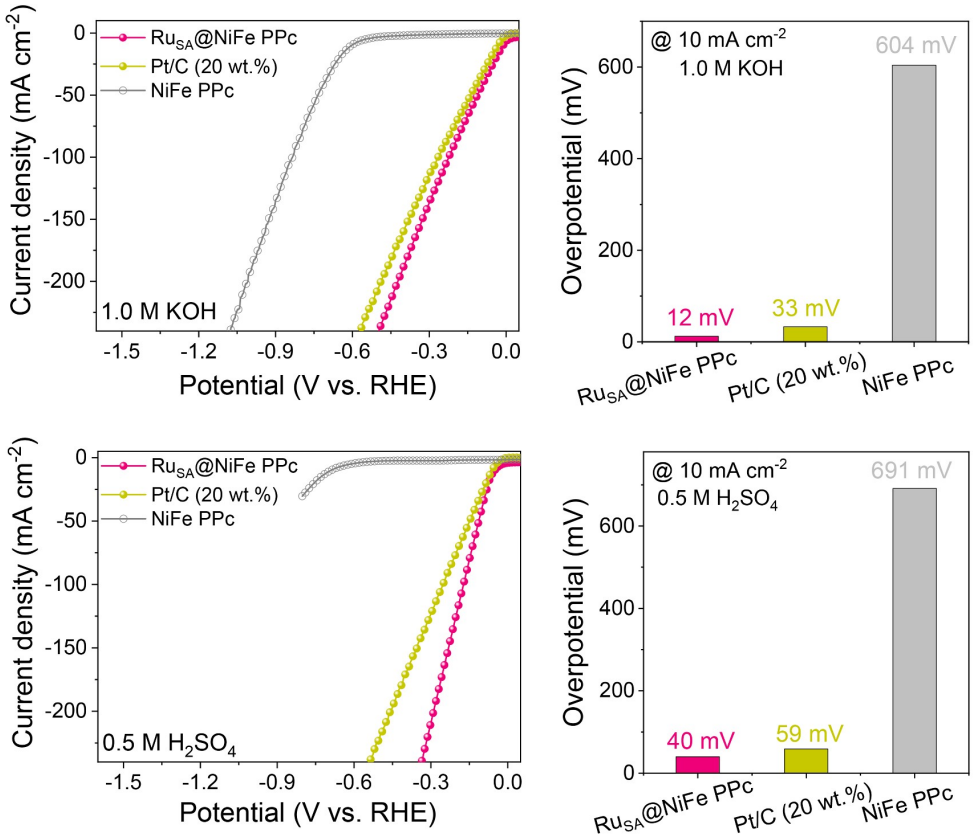

Figure S13. Polarization curves and corresponding overpotentials at current density of 10 mA cm^{-2} of Ru_{SA}@NiFe PPc, Pt/C and NiFe PPc in 1.0 M KOH and 0.5 M H_2SO_4.

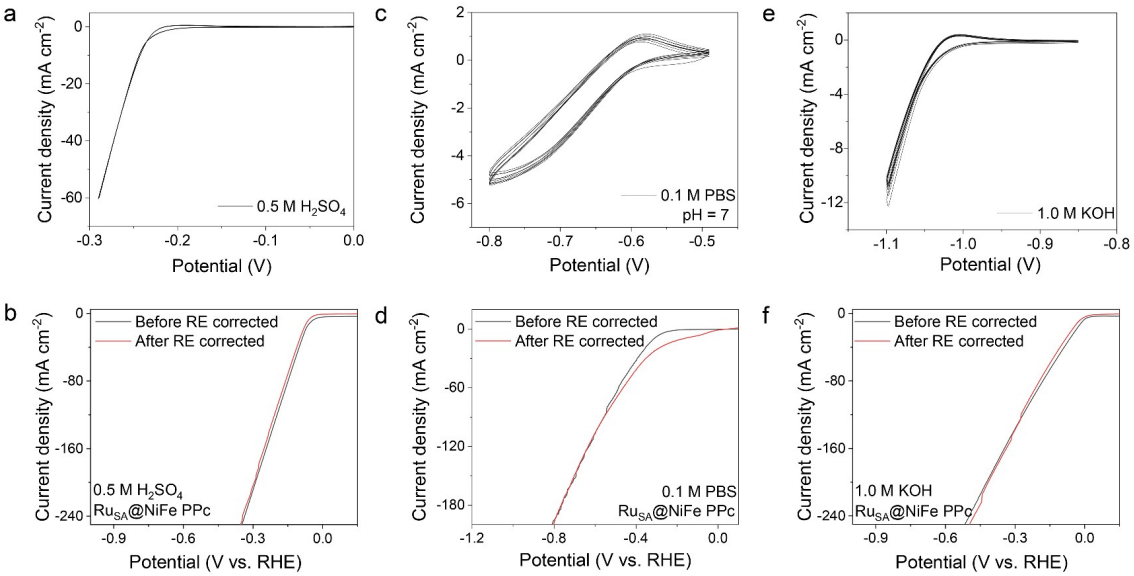

Figure S14. CV curves for calibration of the reference electrode in (a) 0.5 M H_2SO_4, (c) 0.1 M PBS (pH = 7), and (e) 1.0 M KOH. Polarization curves before and after calibration of the reference electrode in (b) 0.5 M H_2SO_4, (d) 0.1 M PBS (pH = 7), and (f) 1.0 M KOH.

A reversible hydrogen electrode (RHE) was used as zero potential point, Ag/AgCl electrode as reference electrode, RHE electrode as working electrode, and platinum plate electrode as counter electrode to form a three-electrode system. Owing to the RHE potential setting as zero point, the potential of the reference electrode was inversely calculated to achieve the purpose of Ag/AgCl calibration. Specifically, a certain range near the open circuit potential (e.g., setting 0 V - -0.29 V in 0.5 M H_2SO_4, -0.49 V - -0.8 V in 0.1 M PBS (pH = 7), and -0.85 V - -1.1 V in 1.0 M KOH) was selected for CV testing with a scanning speed of 1 mV s^{-1}. Next, the two potentials corresponding to the zero current density were selected and averaged, which was the corrected reference electrode potential value. It was worth nothing that the standard Ag/AgCl electrode potential was 0.197 V vs. RHE. After completing the calibration of Ag/AgCl, we re-evaluated the HER activity of Ru_{SA}@NiFe PPc in 0.5 M H_2SO_4, 0.1 M PBS, and 1.0 M KOH, respectively. Clearly, the Ru_{SA}@NiFe PPc still exhibited high performance and almost overlapped with the HER activity before calibration of the Ag/AgCl.

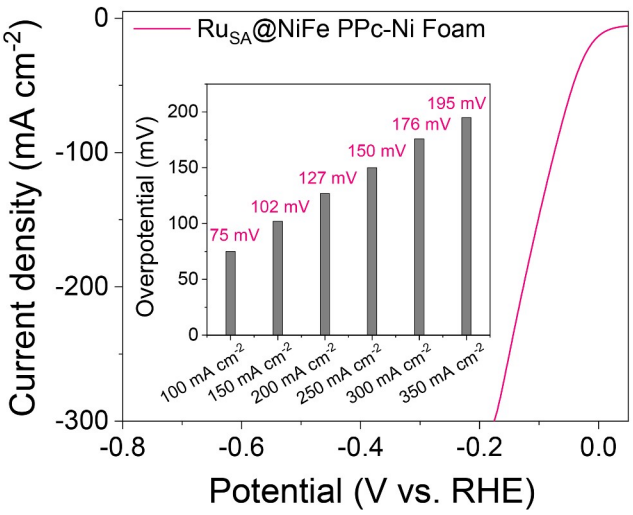

Figure S15. Polarization curve and related overpotential table of Ru_{SA}@NiFe PPc in 1.0 M KOH.

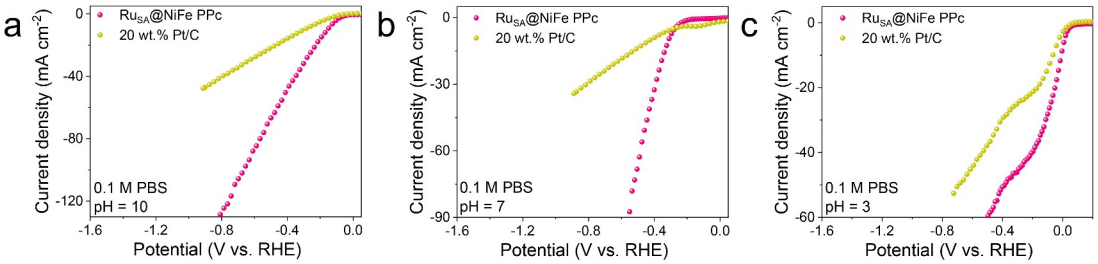

Figure S16. Polarization curves of Ru_{SA}@NiFe PPc and Pt/C in 0.1 M PBS (a) pH=10, (b) pH=7, and (c) pH=3.

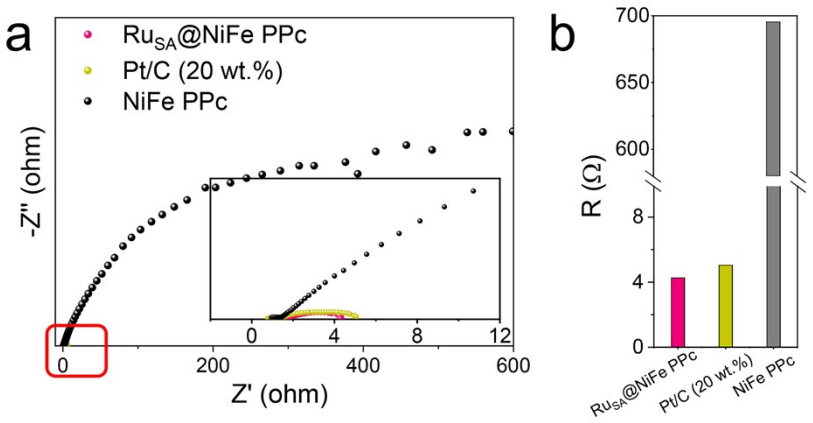

Figure S17. The EIS Nyquist plots (a) and corresponding values (b) of Ru$_{SA}$@NiFe PPc, NiFe PPc, and Pt/C.

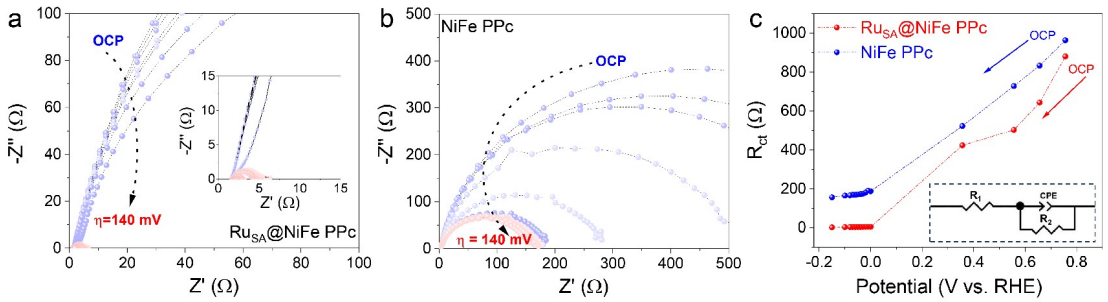

Figure S18. Nyquist plots for (a) Ru_{SA}@NiFe PPc and (b) NiFe PPc at different applied potentials from OCP to 140 mV overpotential. (c) Response of the ion adsorption resistance (R_{ct}) at different potentials for Ru_{SA}@NiFe PPc and NiFe PPc.

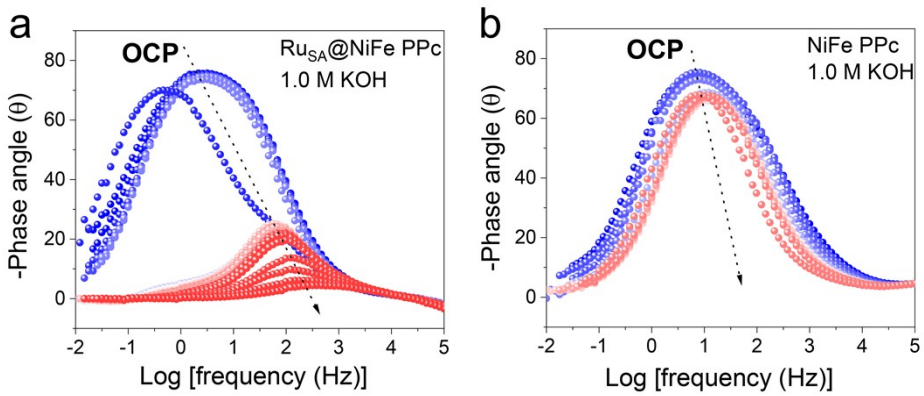

Figure S19. Bode phase plots for (a) Ru_{SA}@NiFe PPc and (b) NiFe PPc.

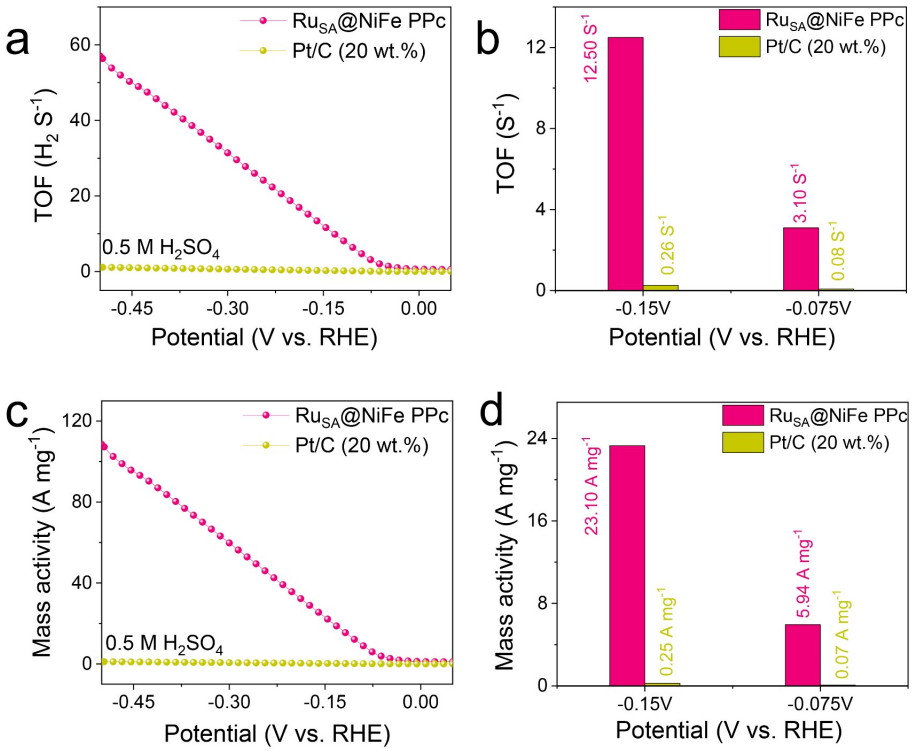

Figure S20. (a-b) Calculated TOF and (c-d) mass activity values of Ru_{SA}@NiFe PPc, and Pt/C in 0.5 M H_2SO_4.

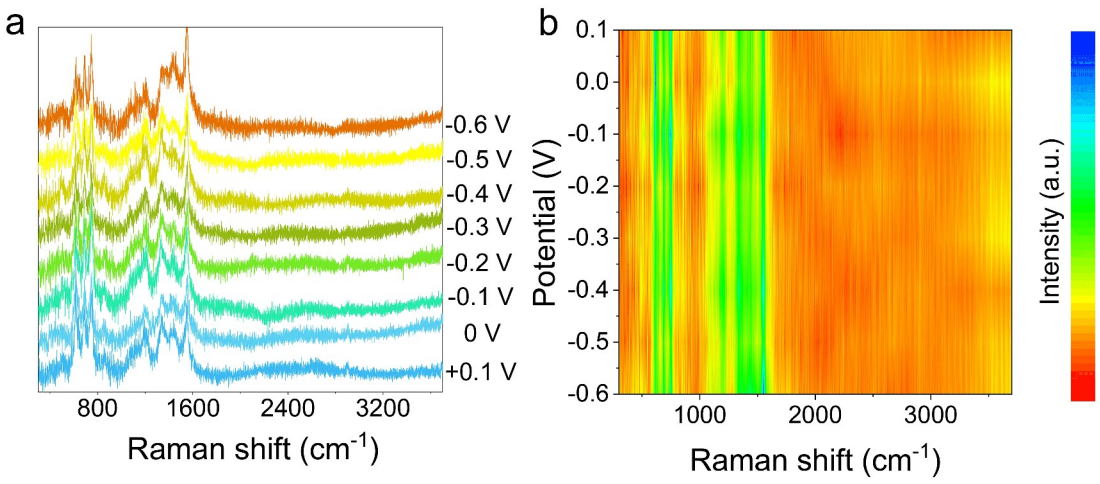

Figure S21. *In-situ* Raman spectra of Ru_{SA}@NiFe PPc.

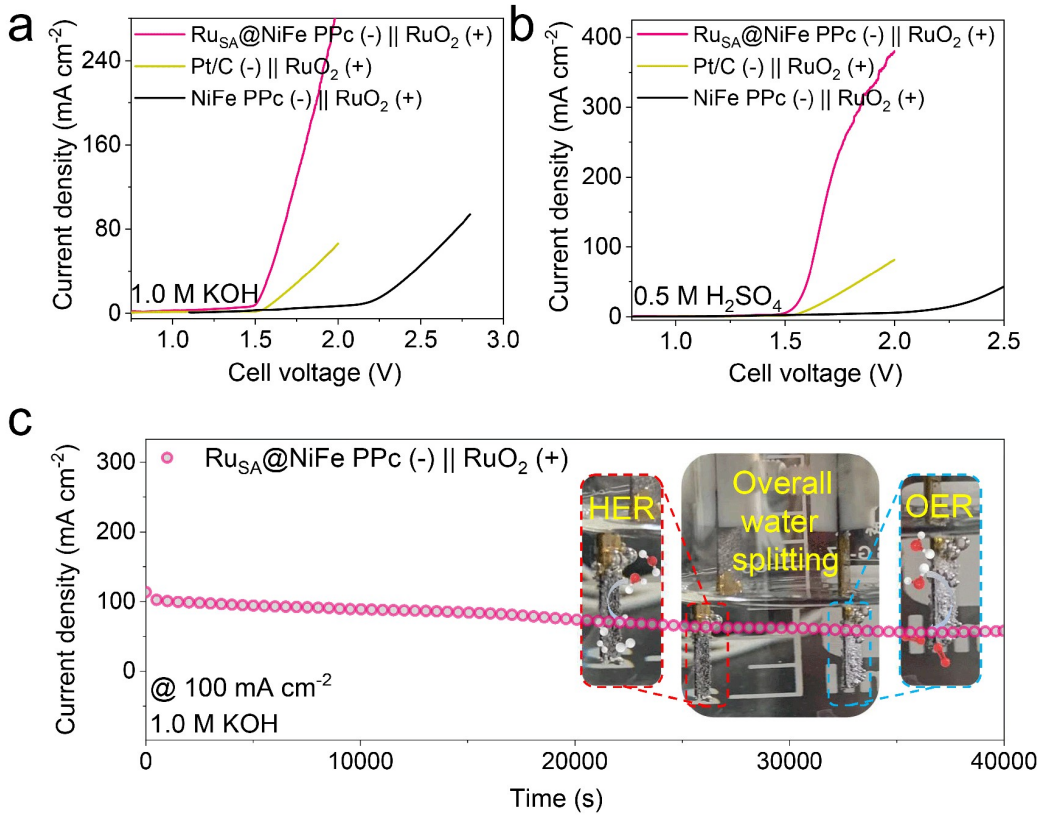

Figure S22. (a) and (b) Polarization curves of overall water splitting for Ru_{SA}@NiFe PPc (-) || RuO_2 (+), Pt/C (-) || RuO_2 (+), and NiFe PPc (-) || RuO_2 (+) in 1.0 M KOH and 0.5 M H_2SO_4, respectively. (c) Amperometric i-t measurement of Ru_{SA}@NiFe PPc (-) || RuO_2 (+) in 1.0 M KOH.

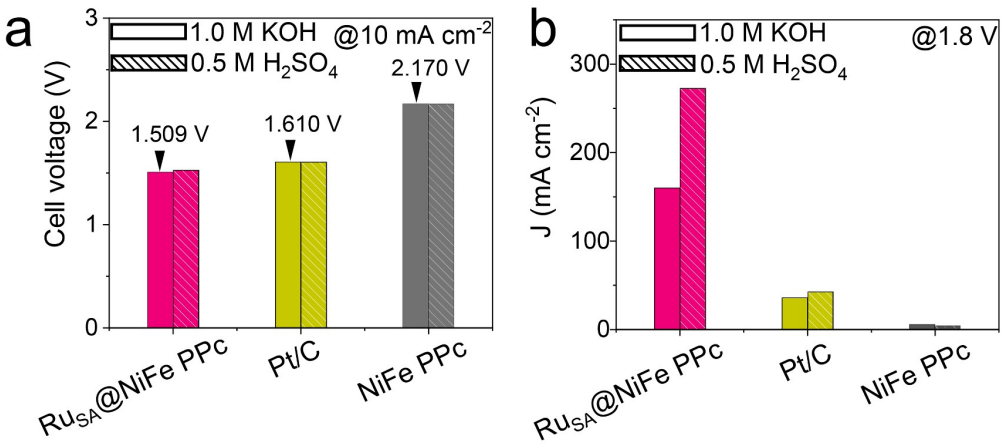

Figure S23. (a) The cell voltages of different overall water splitting systems at 10 mA cm^{-2} in 1.0 M KOH and 0.5 M H_2SO_4, respectively. (b) The current densities of different overall water splitting systems at cell voltage of 1.8 V in 1.0 M KOH and 0.5 M H_2SO_4, respectively.

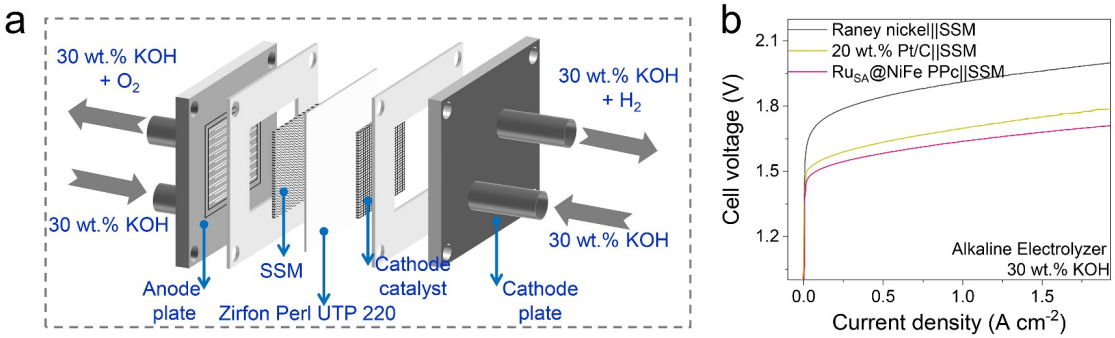

Figure S24. (a) The diagram of alkaline electrolyzer configuration. (b) Polarization curves of Ru_{SA}@NiFe PPc||SSM, Pt/C||SSM, and Ranry nickel||SSM systems in alkaline electrolyzer.

Table S1. Comparison of HER performances between Ru_{SA}@NiFe PPc and other reported noble-metal-based electrocatalysts in alkaline or acid medium.

Catalyst	Electrolyte	Overpotential at 10 mA cm^{-2} [mV]	Mass activity [A mg^{-1}] @ overpotential	Ref.
Ru_{SA}@NiFe PPc	**1.0 M KOH**	**12**	**19.00@150 mV**	**This work**
Ru-$NiCo_2S_4$	1.0 M KOH	32	—	[6]
Ru1/D-NiFe LDH	1.0 M KOH	18	14.65@100 mV	[7]
Pt@DG	1.0 M KOH	37	6.78@100 mV	[8]
Co@CNTs|Ru	1.0 M KOH	10	3.71@10 mV	[9]
Pt/S-TiN NTs/Ti	1.0 M KOH	39	20.3@100 mV	[10]
(N-Ru)@Pt	1.0 M KOH	15	—	[11]
NCAG/Ru-3	1.0 M KOH	4	38.1@100 mV	[12]
$Pt_{0.47}$-Ru/Acet	1.0 M KOH	17	1.33@100 mV	[13]
Ru/g-C_3N_4-C-TiO_2	1.0 M KOH	107	—	[14]
Pt_{SA}-Mn_3O_4	1.0 M KOH	24	0.37@50 mV	[15]
CoPt-Pt_{SA}/NDPCF	1.0 M KOH	31	19.30@50 mV	[16]
SA-Ru/Ru NPs/PC	1.0 M KOH	33	4.2@70 mV	[17]
Ru SAs/N-Mo_2C NSs	1.0 M KOH	43	6.44@100 mV	[18]
Ru ADC	1.0 M KOH	18	—	[19]
Ru SAs-Ni_2P	1.0 M KOH	57	1.13@57 mV	[20]
Ru SAs@PN	0.5 M H_2SO_4	24	—	[21]
Ru_{SA}@NiFe PPc	**0.5 M H_2SO_4**	**40**	**23.10@150 mV**	**This work**

Ru_{SA}-N-S-$Ti_3C_2T_x$	0.5 M H_2SO_4	76	—	[22]
Pt@DG	0.5 M H_2SO_4	30	23.64@100 mV	[8]
Co@CNTs|Ru	0.5 M H_2SO_4	32	—	[9]
$Mo_2TiC_2T_x$-Pt_{SA}	0.5 M H_2SO_4	30	8.3@77 mV	[23]
$Ti_3C_2T_x$-Pt_{SA}	0.5 M H_2SO_4	38	23.21@100 mV	[24]
Pt SASs/AG	0.5 M H_2SO_4	12	22.4@50 mV	[25]
Pt_1/OLC	0.5 M H_2SO_4	38	7.40@38 mV	[26]
$Pt_{0.8}$@CN-1000	1.0 M $HClO_4$	13	11.28@100 mV	[27]
$Pt_{0.47}$-Ru/Acet	0.5 M H_2SO_4	28	2.63@100 mV	[13]
Pt_1/NCNS	0.5 M H_2SO_4	50	7.4@50 mV	[28]
K_2PtCl_4@NC-M	0.5 M H_2SO_4	11	5.5@20 mV	[29]
Pt-SA@HG	0.5 M H_2SO_4	13	20.64@50 mV	[30]
Pt-AC/DG-500	0.1 M $HClO_4$	21	11.78@50 mV	[31]

Table S2. Concentrations of Ru species in Ru_{SA}@NiFe PPc determined by ICP-OES analysis.

Sample	Ru
Ru_{SA}@NiFe PPc	2.607 ppm

Table S3. Best fitting EXAFS data for Ru foil, RuO_2, and Ru_{SA}@NiFe PPc.

Sample	Shell	*CN*[a]	*R*(Å)[b]	σ^2(Å^2)[c]	ΔE_0(eV)[d]	*R* factor
Ru foil	Ru-Ru	12	2.67	0.0031	-6.87	0.0070
RuO_2	Ru-O	6.6	1.97	0.0020	-1.72	0.0157
	Ru-Ru1	13.0	3.14	0.0114	-4.09	
	Ru-Ru2	6.9	3.58	0.0028	3.64	
Ru_{SA}@NiFe PPc	Ru-N	10.8	2.02	0.0148	-3.61	0.0033
	Ru-M (Ni or Fe)	1.1	2.60	0.0029	-9.94	

[a]*CN*, coordination number; [b]*R*, the distance between absorber and backscatter atoms; [c]σ^2, Debye-Waller factor to account for both thermal and structural disorders; [d]ΔE_0, inner potential correction; *R* factor indicates the goodness of the fit. S_0^2 was fixed to 0.73. A reasonable range of EXAFS fitting parameters: $0.600 < S_0^2 < 1.000$; $CN > 0$; $\sigma^2 > 0$ Å^2; $|\Delta E_0| < 10$ eV; *R* factor < 0.02.

Table S4. Comparison of HER performances between Ru_{SA}@NiFe PPc and other reported noble-metal-based electrocatalysts in alkaline condition at high current density of 100 mA cm^{-2}.

Catalyst	Electrolyte	Overpotential [mV] at 100 mA cm^{-2}	Ref.
Ru_{SA}@NiFe PPc	**1.0 M KOH**	**75@Ni foam**	**This work**
Ru-$NiCo_2S_4$	1.0 M KOH	200@Ni foam	[6]
Ru1/D-NiFe LDH	1.0 M KOH	61@Ni foam	[7]
Pt@DG	1.0 M KOH	250@glassy carbon	[8]
Co@CNTs|Ru	1.0 M KOH	208@glassy carbon	[9]
Pt/S-TiN NTs/Ti	1.0 M KOH	90@Ti mesh	[10]
(N-Ru)@Pt	1.0 M KOH	>200	[11]
NCAG/Ru-3	1.0 M KOH	125@glassy carbon	[12]
$Pt_{0.47}$-Ru/Acet	1.0 M KOH	135@Ni foam	[13]
Ru/g-C_3N_4-C-TiO_2	1.0 M KOH	>300@glassy carbon	[14]
Pt_{SA}-Mn_3O_4	1.0 M KOH	90@Ni foam	[15]
CoPt-Pt_{SA}/NDPCF	1.0 M KOH	110@glassy carbon	[16]
SA-Ru/Ru NPs/PC	1.0 M KOH	140@glassy carbon	[17]
Ru SAs/N-Mo_2C NSs	1.0 M KOH	>160@glassy carbon	[18]
Ru ADC	1.0 M KOH	210@glassy carbon	[19]
Ru SAs-Ni_2P	1.0 M KOH	>130@glassy carbon	[20]

Table S5. Concentrations of Ni, Fe, and Ru species in electrolyte before and after stability test determined by ICP-OES analysis.

Ru_{SA}@NiFe PPc	Ni	Fe	Ru
Before HER reaction	0.1223 ppm	0.0405 ppm	<0.02 ppm
After HER reaction	0.1609 ppm	0.0508 ppm	<0.02 ppm

References

[1] Kresse, G. *et al.* Efficient iterative schemes for ab initio total-energy calculations using a plane-w11031103e basis set. *Phys. Rev. B.,* 1996, 54, 11169-11186.

[2] Kresse, G. *et al.* From ultrasoft pseudopotentials to the projector augmented-wave method. *Phys. Rev. B.,* 1999, 59, 1758-1775.

[3] Perdew, J. P. *et al.* Ernzerhof. Generalized gradient approximation made simple. *Phys. Rev. Lett.,* 1996, 77, 3865-3868.

[4] Perdew, J. P. *et al.* Accurate and simple analytic representation of the electron-gas correlation energy. *Phys. Rev. B.,* 1992, 45, 13244-13249.

[5] Grimmea, S. *et al.* A consistent and accurate ab initio parametrization of density functional dispersion correction (DFT-D) for the 94 elements H-Pu. *J. Chem. Phys.,* 2010, 132, 154104.

[6] Su, H. *et al.* In situ electronic redistribution tuning of $NiCo_2S_4$ nanosheets for enhanced electrocatalysis. *Adv. Funct. Mater.,* 2022, 32, 2109.

[7] Zhai, P. *et al.* Engineering single-atomic ruthenium catalytic sites on defective nickel-iron layered double hydroxide for overall water splitting. *Nat. Commun.,* 2021, 12, 4587.

[8] Yang, Q. *et al.* Single carbon vacancy traps atomic platinum for hydrogen evolution catalysis. *J. Am. Chem. Soc.,* 2022, 144, 2171-2178.

[9] Chen, J. *et al.* Inner Co Synergizing outer Ru supported on carbon nanotubes for efficient pH-universal hydrogen evolution catalysis. *Nano -Micro Lett.,* 2022, 14, 186.

[10] Yan, J. *et al.* Synergy of platinum single atoms and platinum atomic clusters on sulfur-doped titanium nitride nanotubes for enhanced hydrogen evolution reaction. *Small,* 2022, 2205603.

[11] Luo, M. *et al.* Promoted alkaline hydrogen evolution by an N-doped Pt–Ru single atom alloy. *J. Mater. Chem. A,* 2021, 9, 14941-14947.

[12] He, T. *et al.* Atomically dispersed ruthenium in carbon aerogels as effective catalysts for pH-universal hydrogen evolution reaction. *Chem. Eng. J.,* 2022,

442, 136337.

[13] Chen, Y. *et al.* Plasma-assisted highly dispersed Pt single atoms on Ru nanoclusters electrocatalyst for pH-universal hydrogen evolution. *Chem. Eng. J.,* 2022, 448, 137611.

[14] Li, Z. *et al.* High-density ruthenium single atoms anchored on oxygen-vacancy-rich g-C_3N_4-C-TiO_2 heterostructural nanosphere for efficient electrocatalytic hydrogen evolution reaction. *ACS Appl. Mater. Interfaces,* 2021, 13, 46608-46619.

[15] Wei, J. *et al.* In situ precise anchoring of Pt single atoms in spinel Mn_3O_4 for a highly efficient hydrogen evolution reaction. *Energy Environ. Sci.,* 2022, 15, 4592-4600.

[16] Yang, W. *et al.* Tuning the cobalt-platinum alloy regulating single-atom platinum for highly efficient hydrogen evolution reaction. *Adv. Funct. Mater.,* 2022, 32, 2205.

[17] Hu, Q. *et al.* Electronic structure engineering of single atomic Ru by Ru nanoparticles to enable enhanced activity for alkaline water reduction. *J. Mater. Chem. A,* 2019, 7, 19531-19538.

[18] Yu, J. *et al.* Tailoring the ruthenium reactive sites on N doped molybdenum carbide nanosheets via the anti-Ostwald ripening as efficient electrocatalyst for hydrogen evolution reaction in alkaline media. *Appl. Catal. B,* 2020, 277, 119236.

[19] Cao, D. *et al.* Construction of dual-site atomically dispersed electrocatalysts with Ru-C_5 single atoms and Ru-O_4 nanoclusters for accelerated alkali hydrogen evolution. *Small,* 2021, 17, 2101163.

[20] Wu, K. *et al.* Atomically dispersed Ni-Ru-P interface sites for high-efficiency pH-universal electrocatalysis of hydrogen evolution. *Nano Energy,* 2021, 80, 105467.

[21] Yang, J. *et al.* Efficient and robust hydrogen evolution: phosphorus nitride imide nanotubes as supports for anchoring single ruthenium sites. *Angew. Chem. Int. Ed.,* 2018, 57, 9495-9500.

[22] Ramalingam, V. *et al.* Heteroatom-mediated interactions between ruthenium single atoms and an MXene support for efficient hydrogen evolution. *Adv. Mater.,* 2019, 31, 1903841.

[23] Zhang, J. *et al.* Single platinum atoms immobilized on an MXene as an efficient catalyst for the hydrogen evolution reaction. *Nat. Catal.,* 2018, 1, 985-992.

[24] Zhang, J. *et al.* Single-atom Pt anchored on oxygen vacancy of monolayer $Ti_3C_2T_x$ for superior hydrogen evolution. *Nano Lett.,* 2022, 22, 1398-1405.

[25] Ye, S. *et al.* Highly stable single Pt atomic sites anchored on aniline-stacked graphene for hydrogen evolution reaction. *Energy Environ. Sci.,* 2019, 12, 1000-1007.

[26] Liu, D. *et al.* Atomically dispersed platinum supported on curved carbon supports for efficient electrocatalytic hydrogen evolution. *Nat. Energy,* 2019, 4, 512-518.

[27] Chen, S. *et al.* High-temperature treatment to engineer the single-atom Pt coordination environment towards highly efficient hydrogen evolution. *J. Energ Chem.,* 2021, 59, 212-219.

[28] Li, J. *et al.* Unveiling the nature of Pt single-atom catalyst during electrocatalytic hydrogen evolution and oxygen reduction reactions. *Small,* 2021, 17, 2007245.

[29] Jin, H. *et al.* Simple and scalable mechanochemical synthesis of noble metal catalysts with single atoms toward highly efficient hydrogen evolution. *Adv. Funct. Mater.,* 2020, 30, 2000531.

[30] Sun, Z. *et al.* Atomic-level Pt electrocatalyst synthesized via iced photochemical method for hydrogen evolution reaction with high efficiency. *Small,* 2022, 18, 2203422.

[31] Cheng, Q. *et al.* Carbon-defect-driven electroless deposition of Pt atomic clusters for highly efficient hydrogen evolution. *J. Am. Chem. Soc.,* 2020, 142, 5594-5601.